Article

Valence Electron and Chemical State Analysis of BeM (M = Ti, V) Beryllides by Soft X-ray Emission Spectroscopy

Keisuke Mukai, Ryuta Kasada, Kiyohiro Yabuuchi, Satoshi Konishi, Jae-Hwan Kim, and Masaru Nakamichi

Just Accepted

Valence Electron and Chemical State Analysis of $Be_{12}M$ (M = Ti, V) Beryllides by Soft X-ray Emission Spectroscopy

Keisuke Mukai,[1] Ryuta Kasada,[2]* Kiyohiro Yabuuchi,[1] Satoshi Konishi,[1] Jae-Hwan Kim,[3] and Masaru. Nakamichi[3]

[1] Institute of Advanced Energy, Kyoto University, Gokasho, Uji, Kyoto 611-0011, Japan

[2] Institute for Material Research, Tohoku University, 2-1-1 Katahira, Aoba-ku, Sendai 980-8577, Japan

[3] Fusion Energy Research and Development Directorate, National Institutes for Quantum and Radiological Science and Technology, 2-166 Obuchi, Omotedate, Rokkasho, Aomori, 039-3212, Japan

* Corresponding author: r-kasada@imr.tohoku.ac.jp

Abstract

Be-rich intermetallics (beryllides) have gathered wide attentions to be adopted for high temperature environments, such as an advanced neutron multiplier in fusion reactors. This study reveals the valence electron structure of $Be_{12}M$ (M = Ti,V) by using soft X-ray emission spectroscopy with ultra-high resolution (~0.22 eV). The Be-Kα spectra from the $Be_{12}M$ phases show significantly lower densities of the occupied states near the Be-K edge than thaose of metallic beryllium. Theoretical calculations indicate that changes in the valence electron structure are derived from the large downward shift of the Fermi level in $Be_{12}M$, by at least 0.8 eV. Based on the knowledge of the valence electron structures and the chemical shift, chemical state mappings of BeO and $Be_{12}V$ in the oxidized beryllide specimen were successfully obtained. The approach is applicable for visualization and identification of metallic/oxidized phase in light-element compounds by electron microscope.

1

Introduction

Beryllides are high-strength and lightweight beryllium intermetallics, which have a wide range of industrial applications for high temperature environments, including structural materials for aerospace systems[1] and refractory materials.[2,3] Recently, Be-rich intermetallics, in particular $Be_{12}M$ (M = Ti,V), have attracted increasing attention as neutron multipliers for fusion reactors as a substitute for metallic Be,[4–6] to ensure fuel tritium self-sufficiency using a low threshold energy for the $^9Be(n,2n)$ reaction with fast neutrons. For such applications, $Be_{12}M$ has a significant advantage in oxidation resistance at elevated temperatures,[7,8] which is an important characteristics because of (i) a toxicity of beryllium oxide, (ii) swelling and cracking caused by oxidation,[7] and (iii) undesired hydrogen generation from reactions with H_2O.[9] The last point is of severe concern for the fusion application because it can cause hydrogen explosions in case of a loss-of-coolant accident. Elemental microanalysis by measuring characteristic X-ray is an essential approach in the development of oxidation resistant beryllides. However, low Z (Z: atomic number) elements such as Be ($Z = 4$) are difficult to detect by the conventional approaches using energy- and wavelength- dispersive spectrometers (WDS).

For the fusion application, several studies have reported that the use of $Be_{12}Ti$ as a neutron multiplier is superior to metallic Be in terms of its tolerance to neutron irradiation and tritium retention.[10,11] It is clear that knowledge of the valence electron configuration is vital for understanding the bond nature and ultimately chemical behaviors of beryllide intermetallics. $Be_{12}Ti$ and $Be_{12}V$ beryllides are members of the $Be_{12}M$ (M = Ti, V, Mo, Cr, W, etc.) series, which exhibit tetragonal symmetry within the I_4/mmm space group.[12,13] In the I_4/mmm crystal, Be occupies three distinct atomic sites; the atomic coordinates of Be1, Be2, and Be3 sites are (1/4,1/4,1/4), (x,0,0), and (x,1/2,0), respectively. On the other hand, Ti/V atoms solely occupy the $2a$ lattice site (0,0,0). Previous theoretical studies by density functional theory (DFT) calculations reported defect formation energies for various types of defects

in metallic Be and beryllides.[14,15] The calculated vacancy formation energies at Bei (i = 1,2, 3) sites in

Be$_{12}$Ti and Be$_{12}$V were in the range 1.43–1.64 eV, which were significantly higher than that in metallic

Be (1.09 eV). Such increases of Be vacancy formation energy have also been reported for Be$_{12}$W.[16]

D. V. Bachrin et al. predicted that Be$_{12}$Ti has a lower hydrogen isotope binding energy compared with

that of Be, by at least 0.4 eV.[17] Burr et al. reported that the Be-Fe(-Al) intermetallics have much lower

oxygen affinity than metallic Be by calculating solution energies of oxygen.[18] The electronic structure

and properties of Be$_{12}$Ti were investigated by DFT calculations.[19,20] However, the studies on the

electric structure were performed with disordered hexagonal cell with P_4/mmm symmetry,[21] which is

pointed out to be incorrect and unstable.[13,22] To the best of our knowledge, no experimental

investigation has reported on the electron structure of Be$_{12}$M beryllide (M = Ti, V) until today.

This study aims to (i) clarify the valence electron structure of Be$_{12}$M (M = Ti, V) and (ii) perform

compositional microanalysis of oxidized beryllide based on the information of electron structure. We

here employ a newly developed soft X-ray emission spectrometer (SXES) attached to an electron

probe micro-analyzer (EPMA), which covers a low energy range (50–210 eV) with ultra-high energy

resolutions of 0.22 eV.[23,24] The unique features of SXES allow analyzing the valence electron structure

of light elements, including Be, with the excellent energy resolution. Moreover, it provides a chemical

state mapping that enables the visualization of two-dimensional distributions of crystallographic

phases in a specimen.[25,26] DFT calculations are performed to simulate the density of state (DOS) in

Be$_{12}$M and to directly compare the experimental SXES spectra.

Experimental section

The metallic Be specimen was prepared by the hot pressing method using S65 grade beryllium

powder (Materion Co., Ltd.). The Be$_{12}$M (M = Ti, V) specimens were fabricated by the plasma-

sintering method.[27] For Be-Ti and Be-V beryllide specimens, the starting powders were mixed with

the stoichiometric ratio of $Be_{12}M$ (92.3 at.% Be and 7.7 at.% Ti/V). The mixed powders were cold-pressed at 50 MPa and then plasma-sintered at 1000 °C for 20 min under 50 MPa pressure. The BeO powder (Mitsuwa Co., >99.5%) was cold-pressed at the same pressure and plasma-sintered at 1430 °C for 15 min. The steamed $Be_{12}V$ specimen was prepared by heating a single-phase $Be_{12}V$ sample at 1000 °C for 24 h under 15% H_2O/Ar atmosphere. The specimens were analyzed by a JXA-8500F field emission EPMA by JEOL equipped with WDS and SXES. The acceleration voltages of the scanning electron beam were 5 and 15 kV for the $Be_{12}Ti$ and the $Be_{12}V$ specimens, respectively. Two types of diffraction gratings, JS50XL and JS200N, were used for the energy ranges of 50–170 eV and 70–210 eV, respectively in the SXES analysis.

The DFT calculations were performed using the Perdew–Burke–Ernzerhof (PBE) generalized gradient approximation (GGA) for the exchange and correlation functional implemented in the Vienna ab initio simulation package (VASP).[28–30] For the Be, O, Ti, and V atoms, the valence electron configurations were $1s^2 2s^2$, $2s^2 2p^4$, $3s^2 3p^6 3d^2 4s^2$ and $3s^2 3p^6 3d^4 4s^1$, respectively, in which both the inner- and outer-shell electrons of Be were involved. By using the Monkhorst–Pack scheme, k-points of $10 \times 10 \times 15$, $10 \times 10 \times 9$, and $10 \times 10 \times 7$ were generated for the unit cells of $Be_{12}Ti$ and $Be_{12}V$ (tetragonal; I_4/mmm space group), $2 \times 2 \times 2$ supercell of BeO (hexagonal; $P6_3mc$), and $3 \times 3 \times 3$ supercell of Be (hexagonal; $P6_3/mmc$), respectively. A plane-wave cutoff energy of 600 eV was used for all calculations. Self-consistency was achieved with a tolerance for a total energy of 10^{-5} eV, and the atomic positions were relaxed until the force was less than 0.02 eV Å^{-1}. For the electronic structure analysis, the DOS at 0 K was calculated for Be metal. Partial density of states (PDOS) at 0 K were calculated to obtain the electron states of Be in BeO and $Be_{12}M$ (M = Ti, V). For a direct comparison with a Be-Kα spectrum using the SXES, the energy of the DOS was determined by setting the Be $1s$ band centroid, $E_{\text{Be-}1s}$, to zero. $E_{\text{Be-}1s}$ was calculated as follows;

4

$$E_{\text{Be-}1s} = \frac{\int_{-\infty}^{E_{\max}} E g_{\text{Be-}1s}(E)dE}{\int_{-\infty}^{E_{\max}} g_{\text{Be-}1s}(E)dE}$$

(1)

where $g_{\text{Be-}1s}(E)$ and $E_{\max}$ are the density of states of the Be $1s$ orbitals at E and maximum energy of

the Be $1s$ orbitals, respectively. The DOSs of Be were convoluted with Gaussian functions with a full

width at half-maximum (FWHM) of 0.5 eV. The crystal structure was depicted by VESTA software.[31]

Results and Discussion

Valence electron structure

　　Fig. 1 shows the entire SXES spectra from the Be, $Be_{12}Ti$, and $Be_{12}V$ phases in the Be metal

and beryllide specimens. The first and second orders of the Be-Kα spectra were observed at 109.0 and

54.5 eV, respectively. The first order Be-Kα peak was chosen for the valence electron analysis because

the intensities were higher than those of the second. Peaks of the constituent elements were observed

from the beryllide specimens at 132 eV (V-Lα,β), 146 eV (V-Lη), 149 eV (Ti-Lα,β), 168 eV (V-

Lα,β), and 195 eV (Ti-Lη). In addition, small O peaks were detected from the all three specimens due

to the formation of thin oxide film on the surfaces. The advantage of using the SXES for the energy

resolutions was clearly observed (inset of Fig.1). The asymmetric Be-Kα spectrum obtained by the

SXES exhibited a sharp drop in the electron population at the Fermi edge. Conversely, no sharp band-

edge was seen in the broad and nearly symmetric spectrum by WDS, which was therefore unsuitable

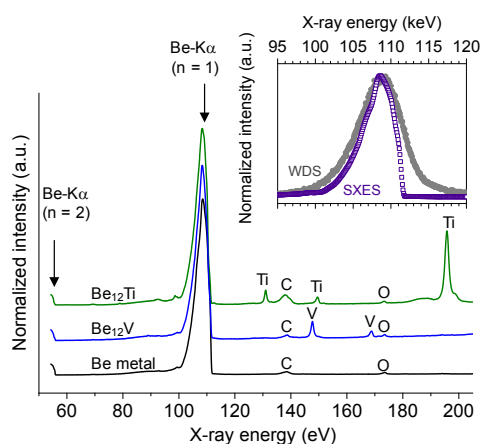for the valence electron structure analysis.

Fig. 1 SXES spectra from Be, $Be_{12}Ti$, and $Be_{12}V$ where n denotes the X-ray diffraction order. Inset plot represents the Be-Kα spectra from the metallic Be specimen by WDS and SXES, showing a difference in the energy resolution.

The results of the EPMA/SXES analyses from the Be-Ti and Be-V beryllide specimens are represented in Fig. 2. The EPMA images (Figs. 2a and 2b) clearly displayed element contrasts related to the atomic mass of the nuclei. In the back scattered electron mode, the phase composed of light elements appeared darker than that of heavy. The EPMA image of the Be-Ti beryllide exhibited Be, Be_2Ti, $Be_{12}Ti$, and Ti phases (Fig. 2a), while Be, Be_2V, $Be_{12}V$, and V phases were observed from the Be-V beryllide specimen (Fig. 2b). The Be-Kα peak intensities from the Be_2Ti and $Be_{12}Ti$ significantly decreased in the energy range 109.0–111.5 eV than that of the Be metal. Significant decreases were also seen for the Be_2V and $Be_{12}V$ phases with a small fourth order V-L peak at 111.7 eV. It is emphasized that the inhomogeneous Be-Ti and Be-V specimens exhibiting the multiple phases were purposely selected for the EPMA-SXES analysis to obtain the spectra from the phases; successful fabrications of the single-phase $Be_{12}Ti$ and $Be_{12}V$ specimens are reported in the previous communications.[32,33]
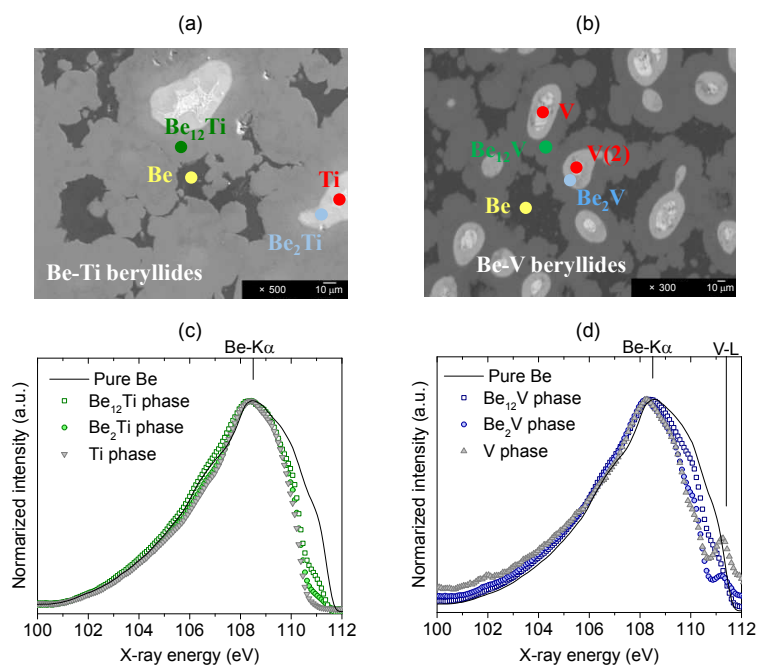
Fig. 2 Surface EPMA images and SXES spectra in the X-ray energy range 100–112 eV from the (a, c) Be-Ti and (b, d) Be-V beryllide specimens. The label "Pure Be" denotes the Be-Kα from the metallic Be specimen.

The lattice parameters obtained by structural optimizations using DFT are listed in Table S1 in Supporting Information (SI). The calculated lattice parameters agreed well with the experimental parameters.[13,34–36] The calculated band gap energy of BeO was 7.2 eV, comparable with the calculated values of 7.0 and 7.54 eV.[37,38] It is noted that the calculated value was largely underestimated compared with that obtained by the experimental (10.6 eV).[39]   Fig. 3 shows the DOS of Be metal and PDOS of Be in $Be_{12}M$ (M = Ti, V) plotted with the energy referenced to the Be 1s band centroid, E_{Be-1s}. The DOS data plotted with the energy referenced to Fermi level (E_F) is shown in Fig. S1 in SI. The FWHM of the Be 1s peaks in $Be_{12}Ti$ and $Be_{12}V$ were 1.0 and 1.1 eV, respectively, which were wider than that of Be 1s in Be metal (0.6 eV). Fig. 4 exhibits partial DOS of each Be site in $Be_{12}Ti$ and metallic Be with the energy referenced with E_F. The wide 1s peaks of $Be_{12}M$ were derived from the strong site dependencies of electronic states among three Be sites in $Be_{12}M$. The Fermi levels of Be,

$Be_{12}Ti$, and $Be_{12}V$ from the $1s$ band centers were 100.0, 99.1, and 99.2 eV, respectively. Namely, the Fermi levels of the beryllides were shifted to lower energies, by 0.9 ($Be_{12}Ti$) and 0.8 eV ($Be_{12}V$) from that of metallic Be. The valence states of Be in the three compounds appeared in the energy range from ~89 eV to the Fermi levels. For the $Be_{12}Ti$ and $Be_{12}V$, the Be $2p$ valence electrons were hybridized with the $3d$ states of Ti and V at the Fermi levels, suggesting covalent bonds of Be–Ti and Be–V (Fig. S2 in SI).
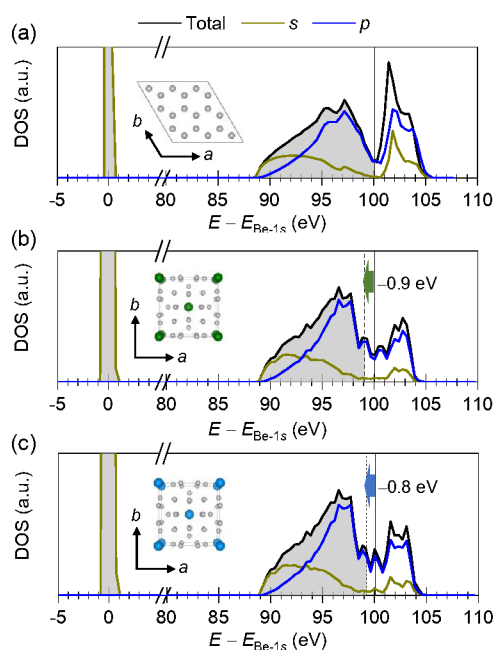
Fig. 3 The DOSs of Be in (a) Be, (b) $Be_{12}Ti$, and (c) $Be_{12}V$ with the energy referenced with $1s$ band centroid, E_{Be-1s}, showing large downward shifts of the Fermi levels in the beryllides. Solid, dotted, and dashed lines represent the Fermi energies of Be, $Be_{12}Ti$, and $Be_{12}V$, respectively. Grey colored area shows the energy regions below the Fermi levels. Be supercell (3×3×3) and unit cells of $Be_{12}Ti$ and $Be_{12}V$ are shown where gray, blue, and green spheres represent Be, Ti, and V atoms.

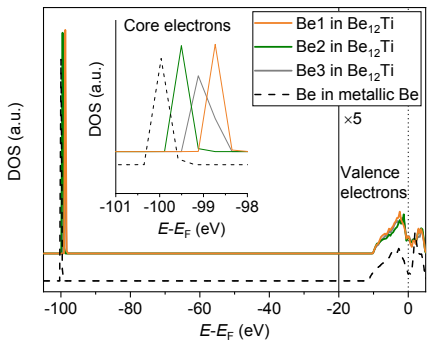Fig. 4 Partial DOSs of Be atoms at Be1, Be2, and Be3 sites in $Be_{12}Ti$ compared with the DOS of metallic Be. The DOS data are plotted with energy referenced to Fermi energy E_F.

The DOSs of Be $2p$ convoluted with the Gaussian functions are directly compared to the Be-Kα spectra using the SXES in Fig. 5. The convoluted Be $2p$ states appeared from 89 to 101 eV, which were ~10% lower in energy compared with those of the experimental spectra. This underestimation of the energy is commonly reported for the PBE approach. The shapes of the convoluted Be $2p$ were in a good agreement with the experimental Be-Kα spectra. The agreement indicates that the SXES spectra dominantly represent the bulk valence electron structures of Be and $Be_{12}M$. The calculations indicated that the significant decrease in the energy range 109.0–111.5 eV may be caused by the large shift of the Fermi levels to lower energies. Shoulders were predicted to appear at 99.0 eV by DFT, representing a 10% underestimation of the energy compared with the shoulders of the SXES spectra at 110.0 eV. This shoulder originates from the hybridization peaks of Be $2p$ with $3d$ of Ti/V at the Fermi levels in $Be_{12}M$. The slight increases in the Be-Kα spectra from the $Be_{12}Ti$ and $Be_{12}V$ phases at 107.0–108.0 eV were seen due to repopulation of valence electrons associated with formation of the intermetallic phases, in consistent with the theoretical valence electron structure.
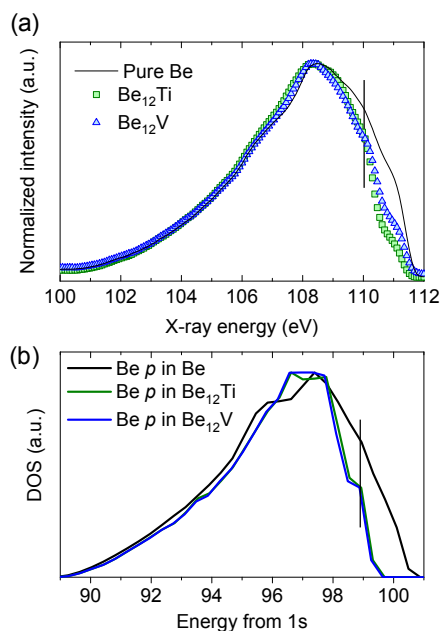
Fig. 5 Direct comparison of the Be-Kα spectra of Be, $Be_{12}V$, and $Be_{12}Ti$ using the SXES with the convoluted DOSs of Be 2*p* by the DFT calculations. Black solid lines represent the shoulders of $Be_{12}Ti$ and $Be_{12}V$.

The Be core electron levels of $Be_{12}Ti$ were positively shifted from that of metallic Be in the DFT calculations (Fig. 4). The difference in the core-levels between Be and $Be_{12}Ti$ derives from the formation for the intermetallic phase, as reported in the previous X-ray photoelectron spectroscopy studies on Be-W intermetallics.[40–42] The calculated binding energies were 98.7 (Be1), 99.5 (Be2), and 99.0 eV (Be3) in $Be_{12}Ti$, which were lower than that of Be atom in metallic Be (100.0 eV). It was confirmed that the binding energies in $Be_{12}V$ are also lower than that of Be in metallic Be (data not shown). This suggests that bond nature of Be, especially at Be1 site, is largely altered by the intermetallic formation associated with the structural change and repopulation of the valence electrons, which may be linked to the altered chemical properties of $Be_{12}M$ (M = Ti, V) beryllides.

Compositional microanalysis

Fig. 6 shows the SXES Be-Kα peak from the BeO specimen and convoluted PDOSs of Be $2p$ in BeO by the DFT calculations, compared with those of Be$_{12}$V. The experimental Be-Kα peak of BeO (Fig. 6a) appeared at 100–108 eV with the peak maximum at 104.5 eV, exhibiting a chemical shift to lower energy as large as 4 eV from the peak maximum of Be$_{12}$V. This SXES spectrum exhibited two additional peaks at 88.5 and 117.5 eV. The peak at 88.5 eV was identified as the hybridization peaks of Be $2p$ and O $2s$, which were predicted to appear at 80.0 eV by the DFT calculation (Fig. 6b). Given that there is a 10% underestimation in a predicted peak position by the computational approach, the SXES peak at 117.5 eV was assigned to the Be $2p$ peak in the conduction band appearing at 106.5 eV. Although the conduction band is theoretically unoccupied states in a pristine metal-oxide, the peak detection could be explained by the accommodation of extra electrons in conduction band of BeO by accelerated electron irradiation during the experiment. The results indicate that a chemical state mapping is feasible by taking advantage of the large chemical shift in Be-Kα between the Be$_{12}$V beryllide and BeO phase. For the following chemical state mapping, P_A, P_B, and P_C were defined as the peak areas in the energy ranges 100–112, 100–106.5, and 106.5–112 eV, respectively (Fig. 6).
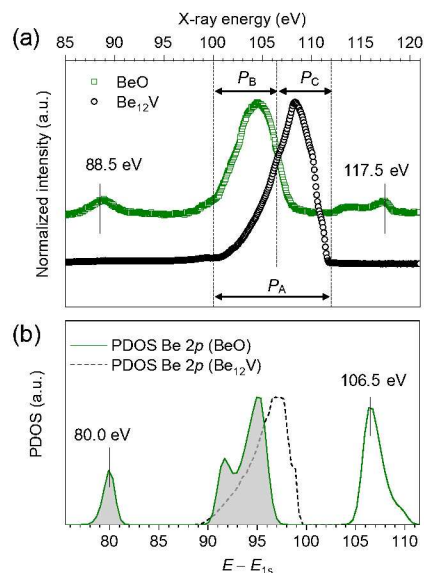
Fig. 6 Chemical shift of Be-Kα of BeO by the SXES (a) and DFT calculations (b) compared with those of Be₁₂V where blue arrows show the energy regions for P_A, P_B, and P_c.
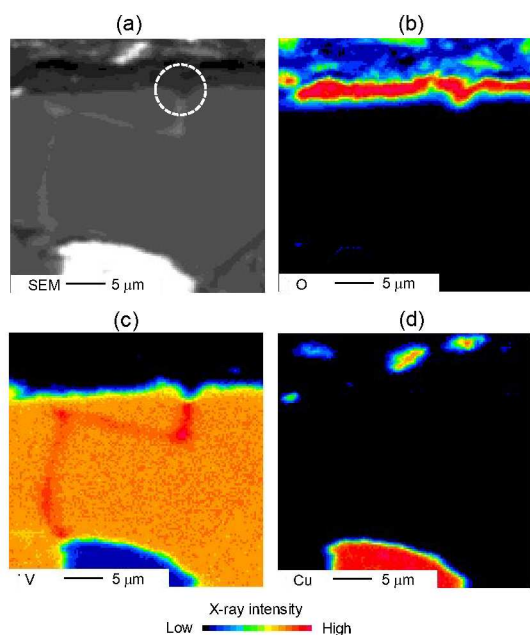

Fig. 7 (a) Scanning electron image and elemental mappings of (b)O, (c) V, and (d) Cu obtained by EPMA-WDS from the cross-section of the steamed Be₁₂V specimen at 1000 °C for 24 h. The white circle in panel (c) represents a hollow observed on the V-rich area.

Fig. 7 shows a scanning electron image and elemental mappings obtained by EPMA-WDS on the cross-section of the steamed $Be_{12}V$ specimen at 1000 °C for 24 h. The element mapping of oxygen clearly shows the formation of an oxidized layer with thickness of a few μm on the surface of the specimen (Fig. 7b). In the matrix, a "N" shaped bright area was observed in the backscatter electron image (Fig. 7a). The V mapping shows the area contained a high amount of V, suggesting an existence of V-rich beryllide such as Be_2V and $Be_{17}V_2$ in the matrix, while an absence of V was observed in the surface oxide layer. An impurity phase was specified as a Cu phase in the resign (Fig. 7d). As the detection limit of the WDS system is atomic number 5 (boron), an element mapping of Be was not obtained. After the EPMA/WDS analysis, the steamed $Be_{12}V$ specimen was subsequently analyzed by SXES. Fig. 8 displays the results of a SXES area scan with 40×32 measuring points on the steamed $Be_{12}V$ specimen. The SXES element mappings of O, V, and Be (Figs. 8a, 8b, and 8c, respectively) were constructed by calculating the signal to noise (S/N) ratios. O, V, and Be peaks were obtained in the energy ranges 173.0–175.5, 100.0–112.0 eV, and 146.0–149.5 eV, while the noise intensity was measured in the energy range 79.0–81.0 eV where no peak appeared (see Fig. 1). As seen in Figs. 8a and 8b, O and V were mainly detected from the oxidized layer and matrix, respectively, as detected by the WDS mappings. As Be distributed in the oxidized layer as well as in the matrix (Fig. 8c), the surface scale was identified to be BeO. In Be element map by the SXES (Fig. 8c), the Be-Kα intensities from the scale was much lower than those from the matrix. This is not because of a difference in elemental concentration, but rather because of a considerable loss of valence electrons by ionization (Be^{2+}) in the oxidized area, as previously observed in the metallic/oxidized lithium specimen.[23] The Be-Kα spectra from the nine measuring points through the scale (Fig. 8d) exhibited BeO peaks at ~105 eV from points 2–5, while $Be_{12}V$ peaks were detected at points 5–9. The measuring point 5, from which a mixed spectrum of BeO and $Be_{12}V$ peak was detected, was positioned at the interface between the surface scale and matrix. The distributions of P_B/P_A (Fig. 8e) and P_C/P_A (Fig. 8f) showed chemical

state mappings of BeO and $Be_{12}V$. The "N" shaped area with a high abundance of V and low Be

concentrations could be Be_2V phase in the matrix. A hollow of the matrix filled with the BeO scale

was observed above the Be_2V area (the circle in Fig. 7c). This hollow can be caused by the faster

oxidation of Be_2V than $Be_{12}V$, based on the phenomena reported for the Be-Ti beryllide.[43] Such phase

identifications of a corroded Be-compound are achieved by the high resolution and the low energy

range of the SXES. With the knowledge of valence electron structure, this novel approach allows a

facile compositional microanalysis regarding to chemical state of Be in an intermetallic/oxidized

beryllide specimen, which is largely beyond the scope of existing approaches such as WDS. The

approach we propose is not only useful for further developments of oxidation resistant beryllide

intermetallics but also applicable for analyzing low Z compounds, for example, identification of

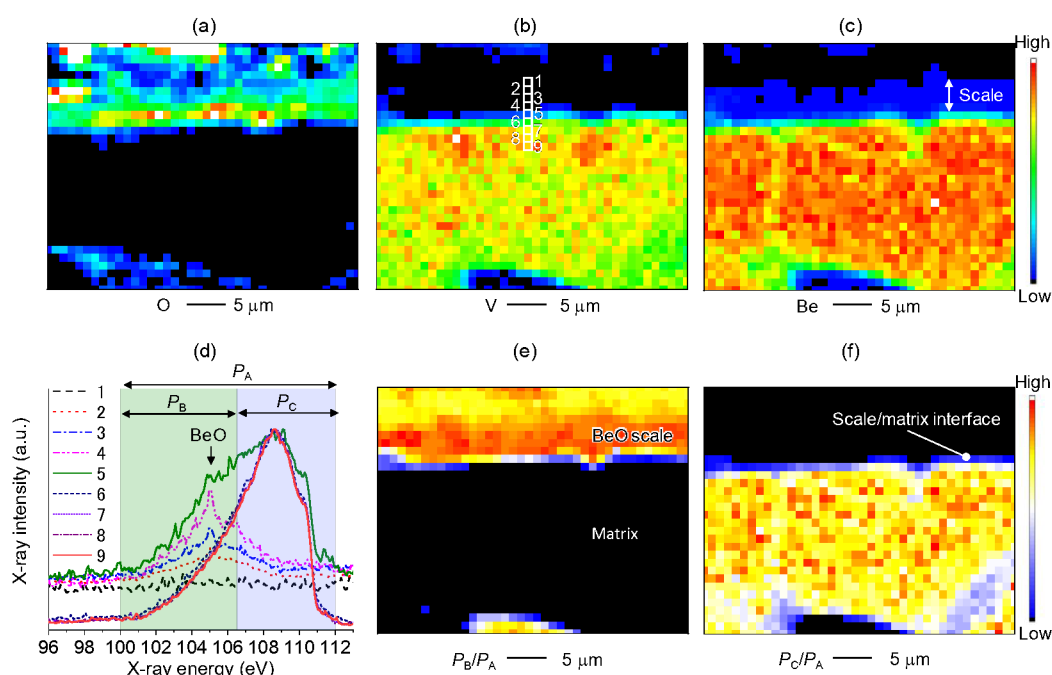metallic and oxidized Li phases in Li-air batteries.

Fig. 8 SXES element mappings of (a) O, (b) V, and (c) Be from the steamed $Be_{12}V$ specimen. (d) The Be-Kα spectra by the SXES from nine measuring area. Reconstructed images by calculating peak area ratio of (e) P_B/P_A and (f) P_c/P_A, showing chemical state mappings of BeO and $Be_{12}V$. In panel (d), nine SXES spectra were obtained from the area surrounded by white squares shown in panel (b).

Conclusion

Valence electronic structures of $Be_{12}M$ (M = Ti, V) beryllide were successfully clarified by EPMA-SXES with ultra-high energy resolutions, for the first time. The Be-Kα spectra (100–112 eV) from the $Be_{12}Ti$ and $Be_{12}V$ phases showed significant decreases in the electron population of the Be $2p$ states for 109–111.5 eV, compared with that from metallic Be. The DFT calculations indicated that the changes are caused by the large shifts of the Fermi levels to lower energy by 0.9 ($Be_{12}Ti$) and 0.8 eV ($Be_{12}V$) as well as the hybridization of the Be $2p$ and V/Ti $3d$ states. Be-Kα from the BeO phase showed a large downward shift compared with those from the intermetallic $Be_{12}M$ phases. It is shown that the chemical state mappings at the micro-scale can be obtained with knowledge of the electron configuration of the beryllide and the scale. This approach overcomes poor sensitivity for low Z elements in conventional method using energy/wavelength dispersive spectrometer and thus useful for analyzing light-element compounds.

Associated content
Supporting Information

Supplementary Information is available free of charge on the ACS Publications website at DOI.

Table S1 and Fig. S1–2 in SI.docx

Author Information
Corresponding authors

Correspondence and requests for materials should be addressed to R. Kasada (r-kasada@imr.tohoku.ac.jp).

15

Notes

The authors declare no competing financial interest.

Reference

1. Bruemmer, S. M.; Arey, B. W.; Brimhall, J. L.; Hirth, J. P. Hot-hardness comparisons among isostructural $Be_{12}X$ intermetallic compounds. *J. Mater. Res.* **1993**, *8*, 1550–1557.

2. J. H. Westbrook. Properties of intermetallic alloys: Vol.III, beryllides and Miscellaneous intermetallic alloys. *Intermetallics* **1998**, *6*, 339–342.

3. T. G. Nieh; J. Wadsworth; C.T. Liu. Hardening behavior of nickel beryllides. *Scripta Metall.* **1988**, *122*, 1409–1413.

4. Vladimirov, P.; Bachurin, D.; Borodin, V.; Chakin, V.; Ganchenkova, M.; Fedorov, A.; Klimenkov, M.; Kupriyanov, I.; Moeslang, A.; Nakamichi, M. Shibayama, T.; van Til, S.; Zmitko, M. Current status of beryllium materials for fusion blanket applications. *Fusion Sci. Technol.* **2014**, *66*, 28–37.

5. Kawamura, H.; Takahashi, H.; Yoshida, N.; Mishima, Y.; Ishida, K.; Iwadachi, T.; Cardella, A.; van der Laan, J. G.; Uchida, M.; Munakata, K.; Sato, Y.; Shestakov, V.; Tanaka, S. Present status of beryllide R&D as neutron multiplier. *J. Nucl. Mater.* **2004**, *329*, 112–118.

6. Konishi, S.; Enoeda, M.; Nakamichi, M.; Hoshino, T.; Ying, A.; Sharafat, S.; Smolentsev, S. Functional materials for breeding blankets—status and developments. *Nucl. Fusion* **2017**, *57*, 092014.

7. Nakamichi, M.; Kim, J. H. Fabrication and hydrogen generation reaction with water vapor of prototypic pebbles of binary beryllides as advanced neutron multiplier. *Fusion Eng. Des.* **2015**, *98*, 1838–1842.

8. Kim, J. H.; Miyamoto, M.; Hujii, Y.; Nakamichi, M. Reactivity and deuterium retention properties of titanium-beryllium intermetallic compounds. *Intermetallics* **2017**, *82*, 20–25.

9. Smolik, G. R.; Merrill, B. J.; Wallace, R. S. Implications of beryllium: steam interactions in fusion reactors. *J. Nucl. Mater.* **1992**, *191*, 153–157.

10. Uchida, M.; Ishitsuka, E.; Kawamura, H. Tritium release properties of neutron-irradiated $Be_{12}Ti$. *J. Nucl. Mater.* **2002**, *307*, 653–656.

11. Kurinskiy, P.; Moeslang, A.; Chakin, V.; Klimenkov, M.; Rolli, R.; van Til, S; Goraieb, A. A. Characteristics of microstructure, swelling and mechanical behaviour of titanium beryllide samples after high-dose neutron irradiation at 740 and 873 K. *Fusion Eng. Des.* **2013**, *88*, 2198–2201.

12. Zalkin, A.; Sands, D. E.; Bedford, R. G.; Krikorian, O. H. The beryllides of Ti, V, Cr, Zr, Nb, Mo, Hf and Ta. *Acta Crystallogr.* **1961**, *14*, 63–65.

16

13. Gillam, E.; Rooksby, H. P.; Brownlee, L. D. Structural relationships in beryllium–titanium alloys. *Acta Crystallogr*. **1964**, *17*, 762–763.

14. Middleburgh, S. C.; Grimes, R. W. Defects and transport processes in beryllium. *Acta Mater*. **2011**, *59*, 7095–7103.

15. Jackson, M. L.; Burr, P. A.; Grimes, R. W. Defect processes in $Be_{12}X$ (X= Ti, Mo, V, W). *Nucl. Fusion*, **2017**, *57*, 086049.

16. Allouche, A.; Fernandez, N.; Ferro, Y. Hydrogen retention and diffusion in tungsten beryllide. *J. Phys*.: *Condens. Matter*. **2014**, *26*, 315012.

17. Bachurin, D. V.; Vladimirov, P. V. Ab initio study of Be and $Be_{12}Ti$ for fusion applications. *Intermetallics* **2018**, *100*, 163–170.

18. Burr, P. A.; Middleburgh, S.C.; Grimes, R.W. Solubility and partitioning of impurities in Be alloys. *J. Alloys Compd*. **2016**, *688*, 382–385.

19. Peng, S. M. Theoretical investigations on the structural, elastic and electronic properties of binary Beryllides under pressure. *J. Nucl. Mater*. **2015**, *464*, 230–235.

20. Liu, X. K.; Zhou, W.; Liu, X.; Peng, S. M. First-principles investigation of the structural and elastic properties of $Be_{12}Ti$ under high pressure. *RSC Adv*. **2015**, *5*, 59648–59654.

21. Raeuchle, R. F.; Rundle, R. E. The structure of $TiBe_{12}$. *Acta Crystallogr*. **1952**, *5*, 85–93.

22. Jackson, M. L.; Burr, P. A.; Grimes, R. W. Resolving the structure of $TiBe_{12}$. *Acta Crystallogr. B* **2016**, *72*, 277–280.

23. Terauchi, M.; Takahashi, H.; Handa, N.; Murano, T.; Koike, M.; Kawachi, T.; Imazono, T.; Koeda, M.; Nagano, T.; Sasai, H.; Oue, Y. Ultrasoft-X-ray emission spectroscopy using a newly designed wavelength-dispersive spectrometer attached to a transmission electron microscope. *J. Electron Microsc*. **2011**, *61*, 1–8.

24. Takahashi, H.; Murano, T.; Takakura, M.; Asahina, S.; Terauchi, M.; Koike, M.; Imazono, T.; Koeda, M.; Nagano, T. Development of soft X-ray emission spectrometer for EPMA/SEM and its application. *IOP Conf. Ser. Mater. Sci. Eng.* **2016**, *109*, 012017.

25. Kasada, R.; Ha, Y.; Higuchi, T.; Sakamoto, K. Chemical State Mapping of Degraded B_4C Control Rod Investigated with Soft X-ray Emission Spectrometer in Electron Probe Micro-analysis. *Sci. rep*. **2016**, *6*, 25700.

26. Takahashi, H.; Handa, N.; Murano, T.; Terauchi, M.; Koike, M.; Imazono, T.; Hasegawa, N.; Koeda, M.; Nagano, T.; Sasai, H.; Oue, Y. Chemical State Mapping via Soft X-rays using a Wavelength Dispersive Soft X-ray Emission Spectrometer with High Energy Resolution. *Microsc. Microanal*. **2013**, *19*, 1258–1259.

27. Nakamichi, M.; Kim, J. H.; Yonehara, K. Novel granulation process of beryllide as advanced neutron multipliers. *Fusion Eng. Des*. **2013**, *88*, 611–615.

28. Perdew, J. P.; Burke, K.; Ernzerhof, M. Generalized gradient approximation made simple. *Phys. Rev*.

lett. **1996**, *77*, 3865–3868.

29. Blöchl, P. E. Projector augmented-wave method. *Phys. Rev. B* **1994**, *50*, 17953–17979.

30. Kresse, G.; Furthmüller, J. Efficient iterative schemes for ab initio total-energy calculations using a plane-wave basis set. *Phys. Rev. B* **1996**. *54*, 11169–11186.

31. Momma, K.; Izumi, F. VESTA 3 for three-dimensional visualization of crystal, volumetric and morphology data. *J. Appl. Crystallogr*. **2011**, *44*, 1272–1276.

32. Nakamichi, M.; Kim, J. H. Homogenization treatment to stabilize the compositional structure of beryllide pebbles. *J. Nucl. Mater*. **2013**, *440*, 530–533.

33. Nakamichi, M.; Kim, J. H.; Miyamoto, M. Fabrication and characterization of advanced neutron multipliers for DEMO blanket. *Nucl. Mater. Energy* **2016**, *9*, 55–58.

34. Schwarzenberger, D. R. Accurate determination of the lattice parameters of beryllium. *Philos. Mag.* **1959**, *4*, 1242–1246.

35. Von Batchelder, F. W.; Raeuchle, R. F. The structure of a new series of MBe_{12} compounds. *Acta Crystallogr*. **1957**, *10*, 648–649.

36. Hazen, R. M.; Finger, L. W. *J. Appl. Phys*. **1986**, *59*, 3728.

37. Chang, K.J.; Froyen, S.; Cohen, M. The electronic band structures for zincblende and wurtzite BeO. *J. Phys. C: Solid State Phys*. **1983**, *16*, 3475.

38. Xu, Y. N.; Ching, W. Y. Electronic, optical, and structural properties of some wurtzite crystals. *Phys. Rev*. B, **1993**, *48*, 4335.

39. Roessler, D. M.; Walker, W. C.; Loh, E. Electronic spectrum of crystalline beryllium oxide. *J. Phys. Chem. Solids* **1969**, *30*, 157–167.

40. Linsmeier, C.; Ertl, K.; Roth, J.; Wiltner, A.; Schmid, K.; Kost, F.; Bhattacharyya, S.R.; Baldwin, M. Doerner, R. P. Binary beryllium–tungsten mixed materials. *J. Nucl. Mater*. **2007**, *363*, 1129–1137.

41. Wang, Y.; Nie, Y.; Pan, L. K.; Sun, Z.; Sun, C. Q. Potential barrier generation at the BeW interface blocking thermonuclear radiation. *Appl. Surf. Sci*. **2011**, *257*, 3603–3606.

42. Ma, Z. S.; Wang, Y.; Huang, Y. L.; Zhou, Z. F.; Zhou, Y. C.; Zheng, W.; Sun, C.Q. XPS quantification of the hetero-junction interface energy. *Appl. Surf. Sci*. **2013**, *265*, 71–77.

43. Kim, J. H.; Nakamichi, M. Oxidation behavior of plasma sintered beryllium–titanium intermetallic compounds as an advanced neutron multiplier. *J. Nucl. Mater*. **2013**, *438*, 218–223.

1
2
3
4
5
6
7
8
9
10
11
12
13
14
15
16
17
18
19
20
21
22
23
24
25
26
27
28
29
30
31
32
33
34
35
36
37
38
39
40
41
42
43
44
45
46
47
48
49
50
51
52
53
54
55
56
57
58
59
60

Table of contents